ELSEVIER

Engineering Analysis with Boundary Elements 22 (1998) 13–31

ENGINEERING ANALYSIS *with* BOUNDARY ELEMENTS

Efficient 2D and 3D electrical impedance tomography using dual reciprocity boundary element techniques[1]

Ramani Duraiswami, Kausik Sarkar, Georges L. Chahine

Dynaflow, Inc., 7210 Pindell School Road, Fulton, MD 20759, USA

Received 14 September 1997; accepted 26 September 1997

Abstract

Numerical algorithms based on boundary element methods are developed for application to problems in Electrical Impedance Tomography (EIT). Two types of EIT problems are distinguished. In the first type internal boundaries of domains of constant conductivity are imaged. For such problems an algorithm based on identifying the shape of the included region is developed, and uses conventional BEM techniques. For problems where a distribution of conductivity is to be imaged algorithms that use dual reciprocity techniques are developed.

The size of the inverse problem required to be solved is much reduced, offering substantial speed-ups over conventional techniques. Further, the present algorithms use simple parametrization of the unknowns to achieve efficiency. Numerical results from tests of this algorithm on synthetic data are presented, and these show that the method is quite promising.

Keywords: Electric impedance tomography; Imaging; Two-phase flows

1. Introduction

In electrical impedance tomography (EIT) the distribution of impedances inside an object ('image') is sought by applying specified currents at some electrodes, and performing measurements of the voltage at other electrodes. The equations for the electric field then provide a relationship between the impedance distribution inside the medium and the measured voltages and applied currents. Different kinds of materials have different impedances, and the availability of an impedance map provides an image of the material distribution. EIT provides an exciting possibility for low-cost imaging, as it uses relatively inexpensive electricity sources for the probing in contrast to the other imaging techniques that rely on nuclear or X-ray radiation or difficult to construct magnetic elements. Since the mid 1980s EIT has seen intense research efforts to develop it into a useful technique for medical and process imaging, and significant progress has been made on the modeling, implementation and use of the technique [1,2].

Impedance tomography techniques are indirect, in that the image must be deduced from voltage measurements which must then be transformed and interpreted to obtain the required image. Achieving this image requires the solution of a non-linear inverse problem, which can only be solved by using iterative techniques. The iterative algorithm for reconstruction as implemented in our study is summarized as follows:

1. Assume a conductivity distribution.
2. Using this distribution, and the applied currents predict the voltage at the measurement electrodes. This is called the *forward problem*.
3. Compare the predicted voltages with the measured values, and determine the error between the measurement and the prediction.
4. Stop if the error is below a specified tolerance. Otherwise generate a new guess for the conductivity distribution using an error minimization procedure, and repeat the iterative steps.

This is illustrated in Fig. 1. The inverse problem is known to be ill-posed [2]. As a consequence up to now one had to accept images of poor quality. Further, classical schemes based on the finite element method (FEM) are often very time consuming, and require extensive computational resources, which make them impractical from an operational viewpoint.

This has led to the wide use of backprojection methods to obtain the image [3], which are based on the idea that the

[1] Supported by NSF grant via grant DMI-9461681 and by DOE Sandia National Laboratories, via contract AO-5480.

0955-7997/98/$19.00
PII: S0955-7997(98)00028-9

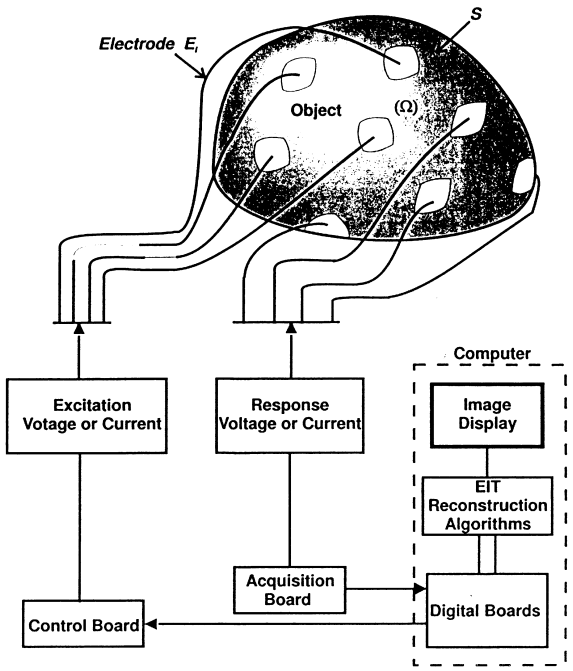

Fig. 1. Notations and operational concept of an Electrical Impedance Tomography experiment.

sought image is a perturbation of a known configuration. However, the backprojection methods are restricted to particular geometries, often provide only qualitative images, and become quite inaccurate when there are large variations of the conductivity in the domain being imaged [4,5,8].

1.1. Approach

1.1.1. Forward problem

Previous investigators have used the finite-element method (FEM) for solving the forward problem. The FEM requires discretization of the whole domain into elements, which are associated with unknown values of the electric potential. Accuracy requires that a large number of elements/variables be used for the discretization. For complex distribution of materials or in three-dimensional problems, a very large number of unknowns is therefore required, and the solution of the forward problem becomes computationally intensive. To increase the efficiency of the solution of the forward problem we employ boundary element methods (BEM).

These methods convert the field equations to integral equations posed on the boundary of the domain, and effectively reduce the dimension of the numerical problem. Only the boundaries of the domain need be discretized, resulting in a considerable reduction in the number of variables required for an accurate solution. The task of meshing the domain is also simplified.

1.1.2. Inverse problem

The solution of the inverse problem, requires 'parametrization' of the impedance, i.e. the distribution of impedance must be represented in terms of a set of parameters. Specification of these parameters determines the impedance distribution. The solution of the inverse problem then consists of determining these parameters. Typically in FEM based approaches, a simple parametrization related to the discretization is used, and the conductivity is treated as unknown on each element [6]. This results in a large minimization problem. Further, new estimates of the conductivity at each iteration require the complete evaluation of the FEM matrices each time the forward problem is to be solved [5]. These factors make the solution of the inverse problem computationally intensive. To reduce the size of the inverse problem we use simpler parametrizations of the unknown conductivities that utilize available a priori knowledge about the problem.

2. Problem equations

Let us consider an Electrical Impedance Tomography problem where we know the current at all of the boundary S of a domain Ω, and the voltage at selected points on the boundary. We have N_E different current patterns applied using M different electrodes. The current in between the electrodes is taken to be zero. The electrical potential at the electrodes is also available. Our objective is to obtain σ, the distribution of conductivity in the material.

The electric potential, ϕ, satisfies the following equation where **n** is the boundary normal [7,20]:

$$\nabla\cdot(\sigma\nabla\phi) = 0 \text{ in } \Omega \tag{1}$$

$$\text{subject to} \begin{cases} \sigma\dfrac{\partial\phi}{\partial n} \text{ and } \phi \text{ measured at the electrodes} \\ \dfrac{\partial\phi}{\partial n} = 0 \text{ on the rest of the boundary.} \end{cases} \tag{2}$$

A direct method for obtaining σ from such measurements is not readily available. Instead, starting from a guessed distribution of σ, a '*forward problem*' is solved. Then, minimization of the error between the predicted and the measured values of ϕ on the boundary is sought for the next guess of the σ distribution, and the procedure is repeated until satisfactory convergence is achieved. Fig. 1 illustrates the problem.

2.1. Formulation of the EIT problem for use with the BEM

For convenience of the BEM formulation, the domain equation is expressed in one of two forms which explicitly display the Laplacian operator in the governing equations. In the first, the equation is represented as

$$\nabla^2\phi = -\nabla \log \sigma\cdot\nabla\phi = b(\mathbf{x}, \phi). \tag{3}$$

In this form the equation is subject to the same boundary conditions as in (2).

The EIT problem can also be formulated as the Helmholtz equation by making the variable transformation, $u=\sqrt{\sigma}\phi$, which leads to

$$\nabla^2 u = ku, \text{ where } k(\mathbf{x}) = \frac{\nabla^2\sqrt{\sigma}}{\sqrt{\sigma}}. \tag{4}$$

To complete the change of variable we must transform the boundary conditions. This variable transformation converts a general linear boundary condition of the form

$$\alpha\phi + \beta\frac{\partial\phi}{\partial n} = f, \text{ to } \left(\alpha - \beta\frac{\mathbf{n}\cdot\nabla\sigma}{2\sigma}\right)u + \beta\frac{\partial u}{\partial n} = \sqrt{\sigma}f. \tag{5}$$

This transformation includes the Dirichlet and Neumann conditions of (2) as special cases.

2.2. Simplified equations for constant conductivity regions

Often the sample to be imaged consists of regions of almost constant conductivity σ_1 embedded in a continuous phase of another almost constant conductivity σ_2. In this case the goal of the imaging is to determine the shape of the interface S_{int}. Since the conductivity is practically constant within each of the materials, the field equation reduces to

$$\nabla^2\phi_i = 0 \text{ in } \Omega, \ i = 1, 2.$$

The boundary condition at the outer surface remains the same as in (2). We must however add the conditions of continuity of the potential and flux at the unknown interface(s) S_{int},

$$\phi_1\Big|_{S_{\text{int}}} = \phi_2\Big|_{S_{\text{int}}}, \ \sigma_1\frac{\partial\phi_1}{\partial n}\Big|_{S_{\text{int}}} = \sigma_2\frac{\partial\phi_2}{\partial n}\Big|_{S_{\text{int}}}. \tag{7}$$

In these problems the forward problem consists of the solution of Laplace equations coupled by boundary conditions of the form (7).

An additional important simplification arises if the interfaces to be imaged enclose materials of vanishing conductivity. Such situations are common in practice, e.g. in determining the distribution of air bubbles in a liquid [9,21,22], or determining the shape of an embedded hollow region by making measurements at an accessible boundary as in non-destructive evaluation of corrosion or cracks in metallic structures. In this special case, the boundary conditions (7) simplify to

$$\frac{\partial\phi}{\partial n} = 0, \text{ on } S_{\text{int}}. \tag{8}$$

It is important to mention that these interface determination problems are ones that traditional FEM based EIT methods find very difficult to solve, as the unknown interface is not naturally treated in these methods, but is accounted for by variation of the conductivity.

3. Forward problem solution using BEM techniques

Solving an EIT problem using a Boundary Element Method (BEM) has the invaluable advantage of considerably reducing computational time especially for three-dimensional problems. Indeed, by requiring discretization of only the boundary, the BEM reduces the dimension of the problem by one, and leads to orders of magnitude reduction in memory and CPU time requirements.

Let us denote the fundamental solution to Laplace's equation by G, so that

$$\nabla^2 G(\mathbf{x},\mathbf{y}) = \begin{cases} 2\pi\delta(\mathbf{x}-\mathbf{y}), \text{ in 2D} \\ 4\pi\delta(\mathbf{x}-\mathbf{y}), \text{ in 3D} \end{cases}$$

$$\text{where } G = \begin{cases} \log|\mathbf{x}-\mathbf{y}|, \text{ in 2D} \\ -|\mathbf{x}-\mathbf{y}|^{-1}, \text{ in 3D} \end{cases} \tag{9}$$

As presented below, (1) and (6) can all be reformulated via *Green's identity*:

$$a\pi\phi(\mathbf{x}) = \int_\Omega \nabla^2\phi(\mathbf{y})G(\mathbf{x},\mathbf{y})dV + \int_S \mathbf{n}\cdot\left[\phi(\mathbf{y})\nabla G(\mathbf{x},\mathbf{y}) - G(\mathbf{x},\mathbf{y})\nabla\phi(\mathbf{y})\right]dS, \tag{10}$$

where $a\pi$ is the angle in 2D (solid angle in 3D) under which the point $\mathbf{x}$ sees the rest of the domain. For formulations with smooth boundaries we typically have:

$$a = \begin{cases} 2, \mathbf{x}\in\Omega \text{ in 2D} \\ 4, \mathbf{x}\in\Omega \text{ in 3D} \end{cases} \quad a = \begin{cases} 1, \mathbf{x}\in S \text{ in 2D} \\ 2, \mathbf{x}\in S \text{ in 3D} \end{cases}$$

3.1. BEM for Laplace's equation

For Laplace's equation (6) the volume integral in (10) vanishes. The surface integrals can then be performed by suitably discretizing the boundaries. In 2D we accomplish this by fitting cubic splines through known points on the boundary, while in 3D we use plane triangular discretizations of the boundary. This enables us to write Green's identity in the form

$$a\pi\phi(\mathbf{x}) = \sum_k \int_{S_k}\left(\phi(\mathbf{y})\frac{\partial G}{\partial n}(\mathbf{x},\mathbf{y}) - G(\mathbf{x},\mathbf{y})\frac{\partial\phi}{\partial n}(\mathbf{y})\right)dS_k. \tag{11}$$

Over each boundary element S_k a linear Lagrangian interpolation of ϕ and $\partial\phi/\partial n$ is performed using the values at the nodes (spline-knots in 2D, triangle vertices in 3D). The resultant boundary integrals can then be performed, leading to a discrete relation between the values of ϕ at points $\mathbf{x}$, and the values of ϕ and $\partial\phi/\partial n$ on the boundary nodes. Following a collocation approach, by selecting the points $\mathbf{x}$ to be the

nodes on S, a linear system of equations of the form

$$\mathbf{A}\frac{\partial\phi}{\partial n}=\mathbf{B}\phi \tag{12}$$

results. Here **A** and **B** are matrices corresponding to the discretization and integration with the Green's function and its derivative. On accounting for boundary conditions at the collocation points, one obtains a closed system of equations, which may be solved for ϕ and $\partial\phi/\partial n$ at the boundary. Knowing these quantities, (10) can be used to obtain ϕ at any other point **x**. The process of discretization, evaluation of the normals, integration (including singular cases when the collocation node lies in the interval of integration), etc. is an involved process. Our treatment of these issues can be found in Refs. [10–12].

3.2. Dual reciprocity method

For equations of the type

$$\nabla^2\phi=b(\mathbf{x},\phi,\nabla\phi), \tag{13}$$

substituting for $\nabla^2\phi$ in (10) leads to

$$a\pi\phi=\int_S\left(\phi\frac{\partial G}{\partial n}-G\frac{\partial\phi}{\partial n}\right)dS+\int_\Omega Gbd\Omega. \tag{14}$$

The presence of a non-constant b in the domain integral prevents a boundary-only formulation. To overcome this difficulty and transform (14) into a boundary-only formulation the Dual Reciprocity (DR) method [13,23] is applied. To do so b is expressed in terms of a special set of known basis functions $\{f_j\}, j=1,...,N$.

$$b(\mathbf{x})=\sum_{j=1}^{N}\alpha_j f_j(\mathbf{x}),\ \mathbf{b}=\mathbf{F}\alpha,\ \alpha=\mathbf{F}^{-1}\mathbf{b}. \tag{15}$$

The functions $\{f_j\}$ have the property that for each function $\{f_j\}$ there exists another known function $\{\psi_j\}$ related to it by

$$\nabla^2\psi_j=f_j, \tag{16}$$

i.e. ψ_j is a particular solution of Poisson's equation with f_j as the right hand side. We can use Green's identity (10) for ψ_j and express the domain integral in (14) as

$$\sum_{j=1}^{N}\alpha_j\int_\Omega f_j G dV=\sum_{j=1}^{N}\alpha_j\int_\Omega\nabla^2\psi_j G dV$$
$$=\sum_{j=1}^{N}\alpha_j\left[a\pi\psi_j-\int_S\mathbf{n}\cdot\left(\psi_j\nabla G-G\nabla\psi_j\right)dS\right]. \tag{17}$$

By substituting in (14) we obtain the following boundary only formulation:

$$a\pi\phi=\int_S\left(\frac{\partial G}{\partial n}\phi-G\frac{\partial\phi}{\partial n}\right)ds$$
$$+\sum_{j=1}^{N}\alpha_j\left[a\pi\psi_j-\int_S\left(G\frac{\partial\psi_j}{\partial n}-\psi_j\frac{\partial G}{\partial n}\right)dS\right]. \tag{18}$$

Again discretizing the boundaries using K nodes and collocating, the following equation is obtained:

$$a\pi\phi(\mathbf{x}_i)=\sum_{k=1}^{K}\left[B_{ik}\phi_k-A_{ik}\frac{\partial\phi_K}{\partial n}\right]$$
$$+\sum_{j=1}^{N}\alpha_j\left[c\pi\psi_j(\mathbf{x}_i)+\sum_{k=1}^{K}\left(B_{ik}\psi_{kj}-A_{ik}\frac{\partial\psi_{kj}}{\partial n}\right)\right], \tag{19}$$

where $i=1,...,K$. It can be expressed in matrix vector form as

$$\mathbf{B}\phi-\mathbf{A}\frac{\partial\phi}{\partial n}=\left(\mathbf{B}\psi-\mathbf{A}\frac{\partial\psi}{\partial n}\right)\mathbf{F}^{-1}\mathbf{b}. \tag{20}$$

Here **A** and **B** are the same as in (12). On accounting for the boundary conditions we can solve for ϕ and $\partial\phi/\partial n$, on the boundary and subsequently for ϕ everywhere.

In the EIT problem the term **b** depends on the unknown function to be determined (ϕ or u). In this case we also expand ϕ in terms of the same set of basis functions

$$\phi(\mathbf{x})=\sum_j\beta_j f_j(\mathbf{x}),\ \phi=\mathbf{F}\beta,\ \beta=\mathbf{F}^{-1}\phi. \tag{21}$$

By using (15) and the gradient of (21) the right hand side **b** in (3) can be interpolated as:

$$\mathbf{b}=-(\nabla h\cdot\nabla\mathbf{F})\mathbf{F}^{-1}\phi$$
$$=-\left[\left(\frac{\partial h}{\partial x}\frac{\partial\mathbf{F}}{\partial x}+\frac{\partial h}{\partial y}\frac{\partial\mathbf{F}}{\partial y}+\frac{\partial h}{\partial z}\frac{\partial\mathbf{F}}{\partial z}\right)\mathbf{F}^{-1}\right]\phi=\mathbf{H}\phi, \tag{22}$$

where $h=\log\sigma$, and the term in square brackets indicates a term by term product of the quantities. This enables us to interpolate the right hand side using values of ϕ at a chosen set of collocation points, with **H** the interpolation matrix.

For the formulation of (4) **b** can be interpolated as:

$$\mathbf{b}=\left[\mathbf{k}\mathbf{F}^{-1}\right]\mathbf{u}=\mathbf{H}\mathbf{u}, \tag{23}$$

where **k** is a vector containing the values of $k=\nabla^2\sqrt{\sigma}/\sqrt{\sigma}$ at the points at which the domain term is collocated, and the term in square brackets is a term by term product. After substitution of **b** by the appropriate expression (22 or 23), (20) becomes

$$\mathbf{A}\frac{\partial\phi}{\partial\mathbf{n}}=\left[\mathbf{B}-S(k)\right]\phi,\ \text{where}\ \mathbf{S}=\left(\mathbf{B}\psi-\mathbf{A}\frac{\partial\psi}{\partial\mathbf{n}}\right)\mathbf{F}^{-1}\mathbf{H}. \tag{24}$$

3.3. Choice of expansion functions

In the above we assumed that functions for performing the dual-reciprocity expansion, f_j, are available. We use a set of functions proposed by Partridge et al. [13]. These functions are based on the distance between the collocation point and the point of interest, so that

$$f_j(\mathbf{x})=1+|\mathbf{x}_j-\mathbf{x}|. \tag{25}$$

This set of functions is already computed in the BEM algorithm since the Green's function involves $|\mathbf{x}_j-\mathbf{x}|$. These

functions are termed radial functions as they depend only on the radial distance between a point, the center of the function $\mathbf{x}_j$, and the evaluation point $\mathbf{x}$. Good practical convergence properties were demonstrated for these functions [13]. Recently the connection between these functions and the *radial basis functions*, an area of active research area in theoretical numerical analysis [14,15], has been established.

3.4. Modification of the algorithms based on numerical tests

3.4.1. Internal nodes

Our tests to date with the DRBEM code developed (described below) showed that when b depends on ϕ and/or its derivatives the accuracy of the solution suffers if b or ϕ show considerable variation inside the problem domain. In these cases we have found that the addition of a few internal points improves significantly the accuracy of interpolation of the right hand side and enables the method to become very accurate, as is necessary for its use in EIT.

Therefore, we add K_I internal points to the K boundary collocation points. Collocating the equation at the K boundary points yields,

$$a\pi\phi(\mathbf{x}_i) = \sum_{k=1}^{K}\left[B_{ik}\phi_k - A_{ik}\frac{\partial\phi_k}{\partial\mathbf{n}}\right] + \sum_{j=1}^{K+K_\mathrm{I}}\left[c\pi\psi_j(\mathbf{x}_i) + \sum_{l=1}^{K}\left[-A_{il}\frac{\partial\psi_{lj}}{\partial\mathbf{n}} + B_{il}\psi_{lj}\right]\right] \times \sum_{k=1}^{K+K_\mathrm{I}} H_{jk}\phi_k. \tag{26}$$

To close the system of equations we need K_I additional equations for the new ϕ_k. This can be obtained by writing Green's identity with $\mathbf{x}$ taken to be at the internal points. Collocating at the K_I internal points we obtain equations formally similar to (26), except that the quantity a takes on the value appropriate to an internal point. We can then write (26) symbolically as

$$\begin{bmatrix} B_{11} & 0 \\ \tilde{B}_{21} & a\pi\delta_{ij} \end{bmatrix}\begin{Bmatrix} \phi_B \\ \phi_I \end{Bmatrix} - \begin{bmatrix} S_{11} & S_{12} \\ S_{21} & S_{22} \end{bmatrix}\begin{Bmatrix} \phi_B \\ \phi_I \end{Bmatrix} = \begin{bmatrix} A_{11} & 0 \\ A_{21} & 0 \end{bmatrix}\begin{Bmatrix} \dfrac{\partial\phi_B}{\partial n} \\ 0 \end{Bmatrix}. \tag{27}$$

We must emphasize that the number of internal nodes that are needed is quite small — at most of the same order as the number of boundary nodes. The feature that makes BEM attractive when compared with domain based methods (such as FEM) still holds, as the internal nodes cause at most a doubling of the number of nodes, while the latter methods require many more nodes to discretize the full space and approximate the differential operators there.

3.4.2. Helmholtz formulation

Our tests during this study also showed that of the two formulations available to solve the EIT equation using the DRBEM, the Helmholtz formulation was more accurate. We suspect that this is due to the fact that the computation of the S matrix in (20) in the former case requires a computation of the derivatives of ϕ using the interpolation. While good interpolation of a function can be achieved using the radial functions (25), the derivatives do not appear to be interpolated as well. Further investigation of this issue is needed. The Helmholtz formulation does not require computation of the derivatives of ϕ. Our Helmholtz formulation codes, transparently perform the variable and boundary condition transformations required to convert from ϕ to $u=\sqrt{\sigma}\phi$ during the solution, and convert back to ϕ for output, or for comparison with the 'experimental data' during the inverse problem solution.

3.4.3. Flow chart

A schematic flow chart for the Dual-Reciprocity BEM codes is shown in Fig. 2. This flow chart illustrates the use of the program both to solve the forward problem, and as a program that is repeatedly called with different σ distributions for evaluation of the error. For a given geometry, most of the computational work is in the evaluation of the matrices $\mathbf{A}$, $\mathbf{B}$, $\mathbf{\Psi}$, $\partial\mathbf{\Psi}/\partial n$, $\mathbf{F}^{-1}$, and the matrix product $[\mathbf{B\Psi} - \mathbf{A}\partial\mathbf{\Psi}/\partial n]\mathbf{F}^{-1}$. These operations take up typically more than 80% of the solution time. For the same computational grid, these only need to be performed once. Subsequent calculations, with different guessed values of the conductivity, just involve the LU decomposition of a single matrix, the formation of the right hand side and the back substitution solution of a linear system. Further speed up is obtained, when we obtain the error corresponding to several experiments with the same σ distribution. In this case the problem requires the solution of the same decomposed system with several right hand sides.

4. The inverse problem

4.1. Objective function for minimization

With the EIT experiments as described earlier, we have N_E experiments in which the current is known at all of the boundary, and the potential is known at M electrodes. The quantity to be imaged is described through a parametrization by P quantities, arranged in the vector $\mathbf{p}$. We further know that the correct solution to the problem, $\phi^{(k)}$, satisfies the following boundary conditions for $k = 1,...,N_\mathrm{E}$,

$$\frac{\partial\phi^{(k)}}{\partial n} = g^{(k)} \text{ on } S; \text{ and } \phi^{(k)} = \hat{\phi}_l^{(k)} \text{ on } E_l \;\; l = 1,\ldots,M, \tag{28}$$

where the superscript k refers to a given experiment, E_l to electrode l, and $\hat{\phi}^{(k)}$ refers to the measurements available at the electrodes.

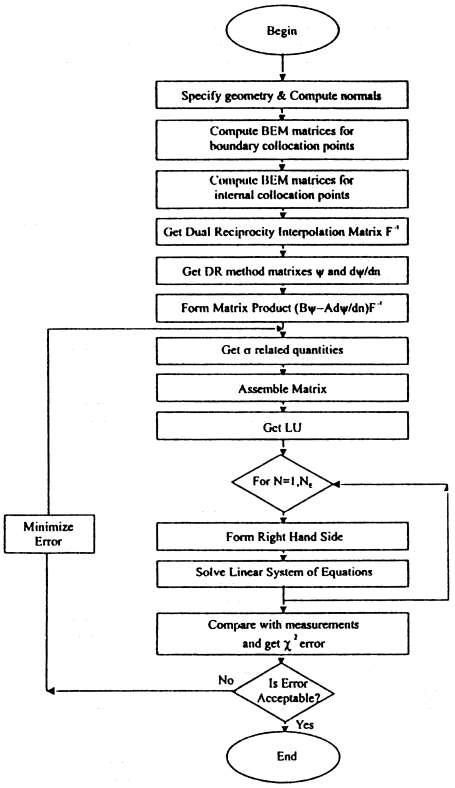

Fig. 2. Flow chart for the DRBEM Codes 2DynaEIT and 3DynaEIT.

Corresponding to the parametrization **p** we have an estimate of the operator of the problem L_p. Using a guessed parameter vector we solve the forward problem expressed as,

$$L_p\tilde{\phi}^{(k)} = 0, \text{ subject to } \frac{\partial\tilde{\phi}^{(k)}}{\partial n} = g, \text{ on } S. \tag{29}$$

We can accordingly form $M \times N_E$ measures of the error

$$e_i = \hat{\phi}_l^{(k)} - \tilde{\phi}_l^{(k)}, \; i = 1, \ldots MN_E, \tag{30}$$

where $\tilde{\phi}_l^{(k)}$ are the value of the computed field $\tilde{\phi}^{(k)}$ at the l-th electrode. We seek the values of **p** that minimizes the above vector of errors.

We use a least-squares approach, which reduces an array of objectives into a single objective function:

$$\chi^2 = \sum_{i=1}^{M\times N_E} \left(\hat{\phi}_i - \tilde{\phi}_i(\mathbf{p})\right)^2. \tag{31}$$

This approach has the disadvantage that it subsumes detailed spatial error distribution information into one all encompassing error function, which can have multiple local minima.

4.1.1. Parametrization of unknowns

The solution of the inverse problem, requires changing the guessed impedance distribution, or the location of the inclusions, to minimize the quantity χ^2. In the conventional FEM approaches for solving the problem, the whole domain is discretized into elements. Typically the conductivity in each of these elements is also treated as an unknown (usually assumed constant over the element). This results in a huge minimization problem. Further, as the conductivity appears in the equations of each element, new estimates of the conductivity at each step require the complete evaluation of the FEM matrices each time the forward problem is to be solved.

4.1.2. Decoupled parametrization

One of the principal advantages of our BEM method for EIT is that it permits a decoupling of the parametrization of the unknown conductivity or surface location from the forward problem discretization. This leads to a significant reduction of the number of parameters in the inverse problem, and enables using a priori information. This has the advantage of mitigating the ill-posed character of the problem. Furthermore, using this approach, we have been able to develop algorithms where most of the computational work that is required for the solution can be performed at the outset, and subsequent solutions of the forward problem are performed using much fewer operations. Since the minimization procedures require solution of many forward problems with different values of the parameters, this approach results in significant speed up of the minimization.

The images achieved by FEM based reconstructions tend to be of poor quality, which require algorithms to sharpen the images. Methods based on total variation minimization, [16] and hyperbolic shock-fitting [17] have been proposed for this in the literature. However, such algorithms would tend to add further to the computational cost of the reconstruction, and further, have the potential of introducing artifacts in the image. Our BEM based approach for looking for sharp interfaces from the start has the advantage of embedding this in the solution procedure.

4.1.3. Parametrization chosen for study

4.1.3.1. Distribution of inside bodies. For preliminary testing of our codes we chose the standard 2D problems of identifying a cylindrical object inside a cylindrical container, on the boundary of which electric measurements are taken. In this case we parametrized the inner circle by the location of its center, and by its radius (3 parameters). The codes were then tested for multiple circles in the inner domain. Of course, the choice of this parametrization is open to the criticism that FEM codes do not assume a specific shape. Accordingly we have also considered single and multiple regions of arbitrary shapes that are each described by a series of Legendre polynomials

$$f(r,\theta) = r_0\left(1 + \sum_{k=1}^{N} r_k P_k(\cos\theta)\right), \tag{32}$$

and the center of the shape, leading to a total of $N + 3$ parameters. For the three-dimensional codes we considered

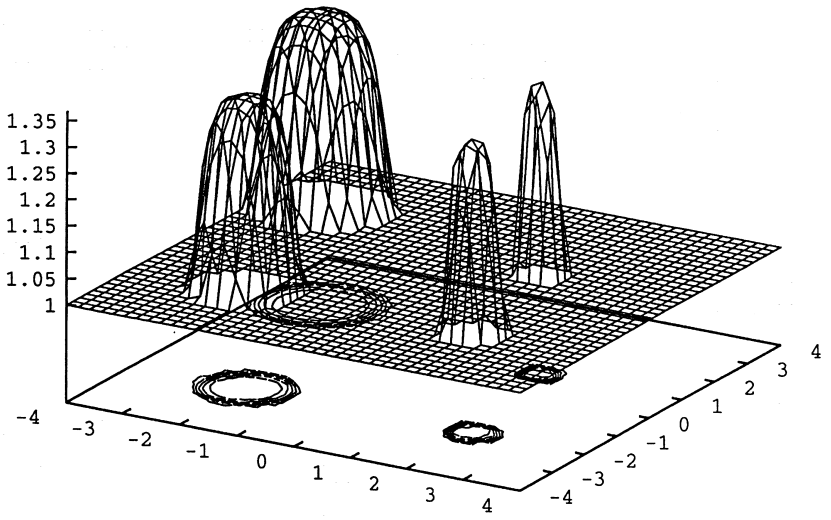

Fig. 3. An example of the parametrization of σ in terms of 4 modified Gaussian functions, on a background of constant conductivity domain. The parametrization includes a priori information on the localized nature of σ variations.

a spherical container that contains single or multiple spheres of zero conductivity. The choice of circular and spherical container is purely for convenience of the set-up of the problem. The codes in their present form are written for any user prescribed shape of the outer boundaries.

4.1.3.2. Conductivity distribution. For problems where a distribution of the conductivity is to be obtained we have chosen a parametrization characterized by sums of local functions on a background constant conductivity σ_c (See Fig. 3).

$$\sigma = \sigma_c + \sum_{j=1}^{L} \sigma_i f_i(\mathbf{x} - \mathbf{x}_i). \tag{33}$$

Function Name	**Expression**
Test function	$\exp\left(\frac{1}{r^2 - a^2}\right) \quad r < a$
	$0 \quad r \geq a$
Gaussian	$\exp(-\alpha r^2)$
Modified Gaussian	$\exp(-\alpha r^n)$
tanh	$\frac{1}{2}(1 + \tanh(n(r - r')))$

The functions f_i include Gaussians, Gaussians of higher power, Test functions, and functions based on tanh(x), and are presented explicitly in the table above. All these parametrizations are able to represent blocky distributions of σ. Also, with this choice the quantity $k(x)$ of (4) can be calculated analytically. We thus are able to analytically obtain the derivatives required for the Helmholtz formulation.

4.2. Constraints on the solution

In solving inverse problems it is quite important to constrain the solution using a priori information to mitigate their ill-posed character. For the present problem, constraints on the geometry of the internal surfaces, or on the localized character of the distribution of σ can be formulated. However, most available non-linear multi-dimensional optimization schemes are formulated for unconstrained problems, and do not permit imposition of additional constraints. As discussed previously our choice of the parametrization of the unknown interfaces or surfaces, introduces some of this a priori information in the form of the function σ, or in the parametrization of S_{int}, without requiring specific additional constraints.

We implemented further constraints in a numerical manner by artificially modifying the error and gradient calculation procedures. For example in the case of a problem where multiple inner surfaces are to be identified, when presented with a configuration that leads to overlapping, or to very large or very small sizes of the inner inclusions, the error evaluating function returns an artificially large value of the error, and a gradient vector set to a unit vector in the direction that leads away from the error. Similar constraints are applied to the cases where the conductivity distribution is being evaluated. In this case, the centers of the radial functions are prevented from coming close to each other, and the value of σ is forced to remain positive.

5. Results for the forward problem

We developed a 2D BEM and a 3D BEM code to the inner interface problem, and developed the dual reciprocity codes **2DynaEIT** and **3DynaEIT**. These codes constitute the tools for the forward problem solution, and are in addition called repeatedly in the inverse problem solution. Sample validation results from these codes are presented below.

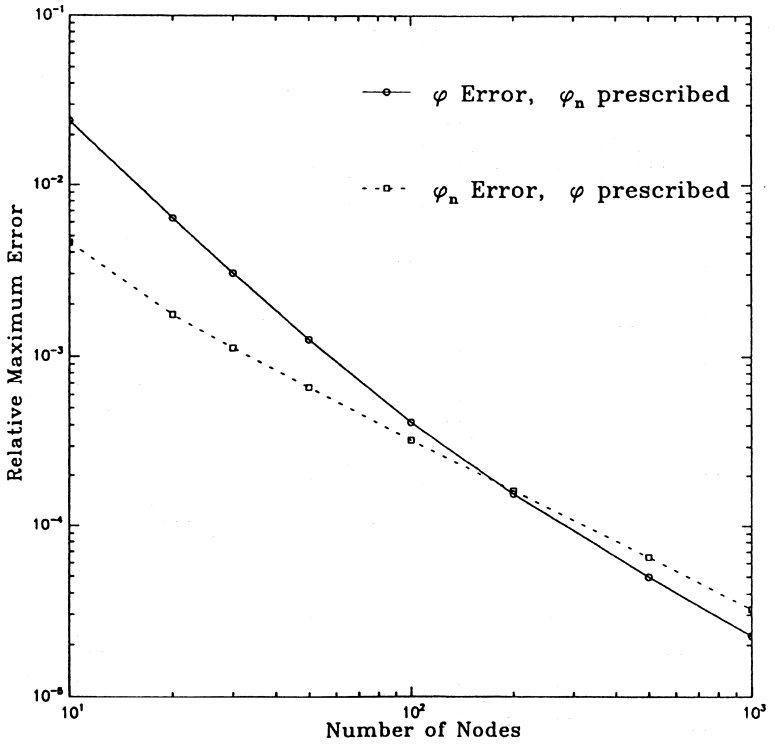

Fig. 4. Influence of discretization on the relative maximum error for a problem involving two concentric circles and a dipole at the origin for the distribution of ϕ.

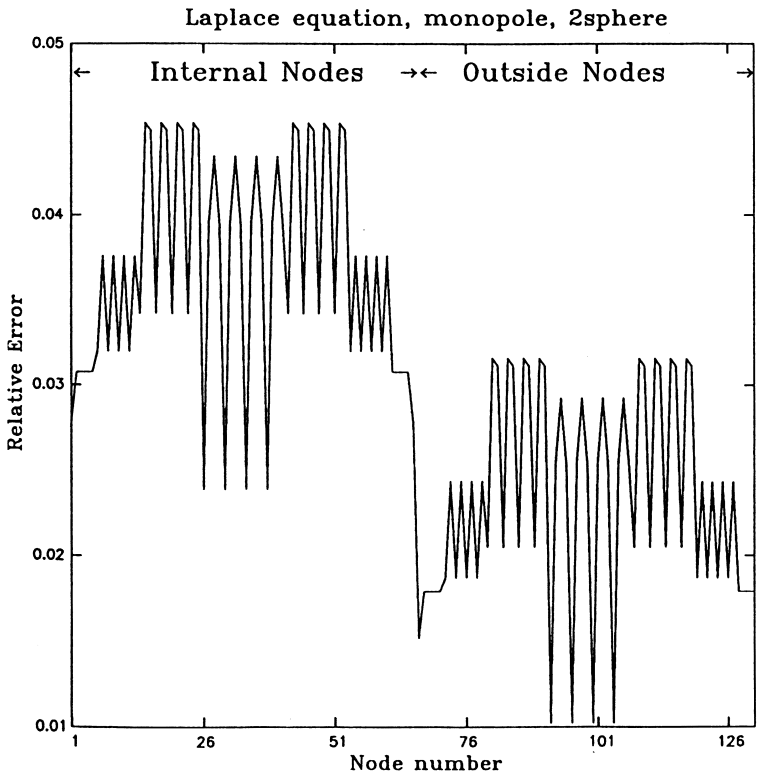

Fig. 5. Distribution of the relative error for a two sphere and a monopole ϕ at the origin. Coarse discretization (66 nodes, 128 panels) problem (R1 = 1, R2 = 4).

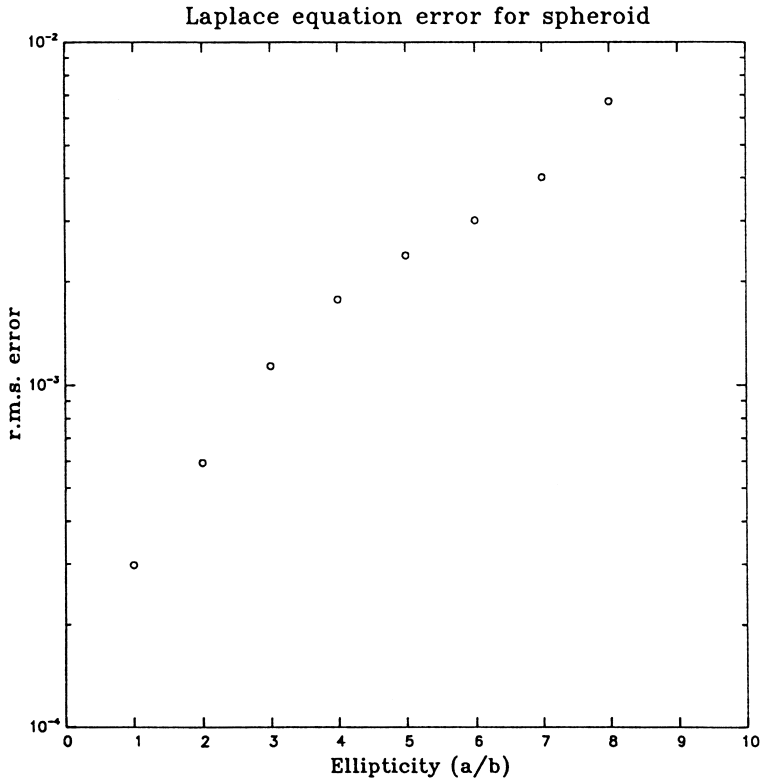

Fig. 6. The r.m.s. error versus ellipticity of a spheroid for a monopole solution in a domain bounded internally by the spheroid.

5.1. Laplace's equation

Fig. 4 illustrates in a particular case the influence of the grid resolution on the maximum relative error achieved by the code for a problem with known analytical solution. The analytical solution chosen was that corresponding to a dipole at the origin, and the problem geometry was that of two concentric circles. The problem was solved with either ϕ or $\partial\phi/\partial n$ prescribed on the boundary, with the other variable calculated. As can be seen the code is able to solve the problem very accurately.

Fig. 5 shows the computed and analytical solution for an imposed monopole like distribution of ϕ using the 3D code. The domain is that bounded by two concentric spheres of radii 1 and 4. Both spheres are discretized with 66 nodes and 128 triangular panels. This is considered a very coarse discretization but leads to errors less than 3%. We prescribed ϕ on the boundary and solved for $\partial\phi/\partial n$. The discretization for a sphere using triangles can be seen in Fig. 19. The error reduces to 1% if the number of nodes and panels is increased to 402 and 800.

To represent the effects of discretization for a non-spherical body we took the same monopole solution and solved a problem on the domain exterior to an spheroid. Again ϕ was prescribed on the spheroid, and $\partial\phi/\partial n$ computed, and compared with the maximum error. The ellipticity a/b, was varied, and the number of nodes and panels kept fixed at 402 and 800 respectively. The value of $\partial\phi/\partial n$ at every node was compared with the analytical value, and the r.m.s. error (the mean over all the nodes) is plotted for varying ellipticity a/b in Fig. 6. Here a is the length of the stretched axis, with the other two axes of length b. With increasing ellipticity the mesh becomes distorted and coarser, and the error increases as expected.

5.2. Dual reciprocity code test

We first developed dual reciprocity codes for the Poisson equation, i.e. where b was a function of position but not of ϕ in (13), and for the simple Helmholtz equation with b given by $-\lambda^2\phi$. These codes were accurate for some problems, but displayed gross inaccuracies when b varied considerably in the domain. These observations led us to the formulation with internal points described earlier.

In Fig. 7, we solved the Helmholtz equation with $\lambda = 0{\cdot}4$ with ϕ given on the boundary. In Fig. 8, the Poisson equation is solved for a right-hand side x^2 with ϕ imposed based on the analytical solution. The computed values of $\partial\phi/\partial n$ at the surface (dotted line) is compared against the known analytical solution (solid line). Fig. 9 shows the same situation as Fig. 7 but with $\lambda = 2{\cdot}0$. Fig. 10 shows a similar case as Fig. 8, except that the right hand side is x^3.

Figs 7 and 8 show examples where the code without internal points performed satisfactorily, while Figs 9 and 10 show cases where the solution was poor. In the 3D cases the problem domain is that bounded by two concentric spheres of radius 4 and 1, both having 66 nodes and 128

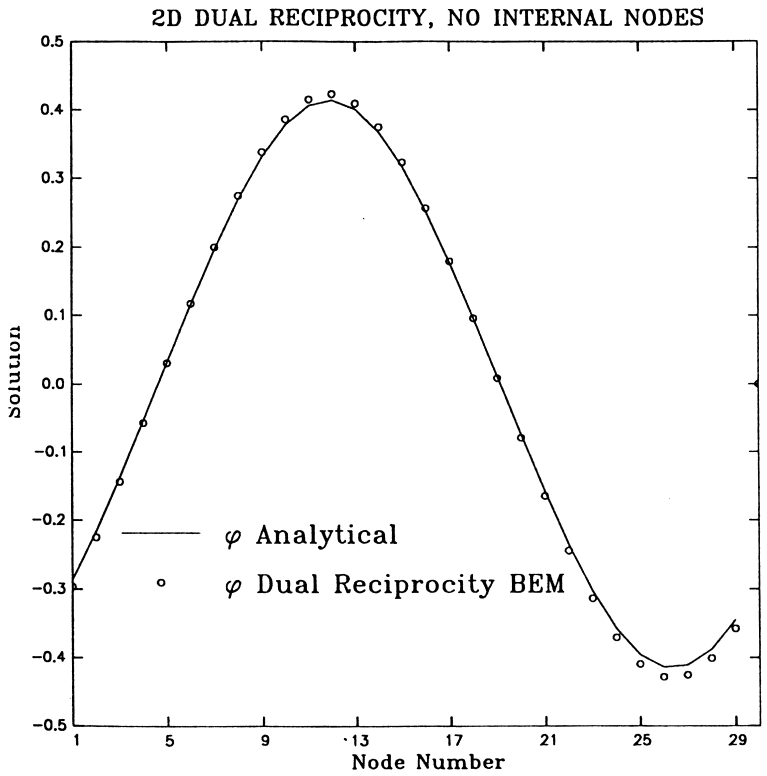

Fig. 7. The solution of the Hemlholtz Equation $\nabla^2\phi = -\lambda^2\phi$ on a unit disk using the 2D DRBEM code. Satisfactory solution is achieved for $\lambda = 0.4$ despite the lack of internal nodes.

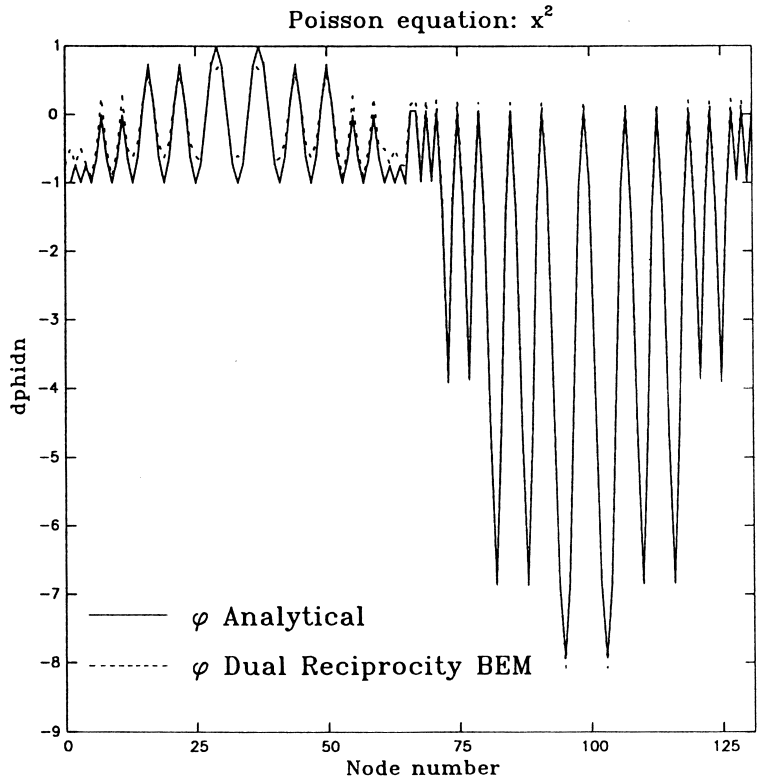

Fig. 8. The solution of the Poisson equation $\nabla^2\phi = x^2$ using the 3D DRBEM code on a domain bounded by two concentric spheres of radius 1 and 3. Satisfactory solution is achieved despite the lack of internal nodes.

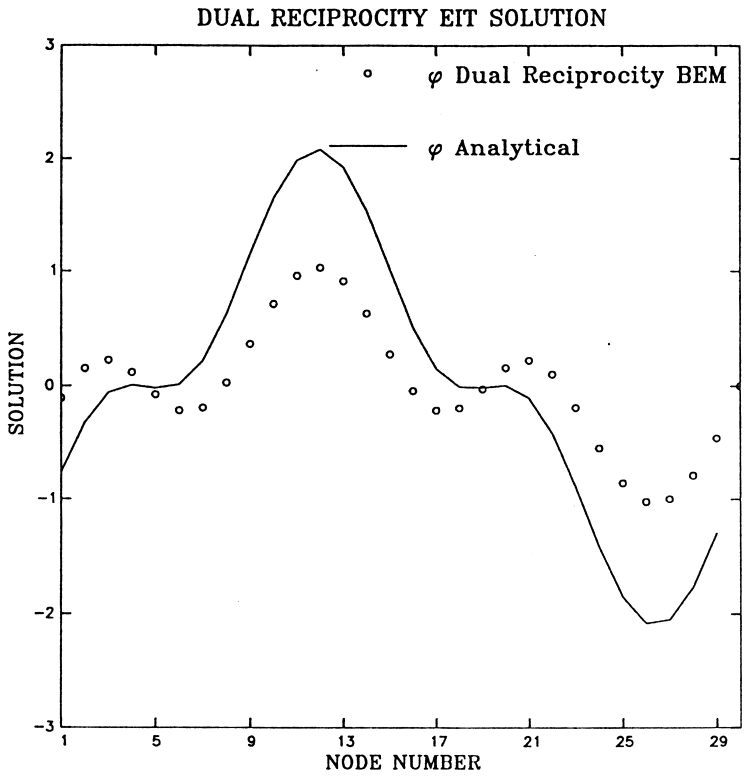

Fig. 9. The solution of the Helmholtz Equation $\nabla^2\phi = -\lambda^2\phi$ on a unit disk using the 2D DRBEM code. For $\lambda = 2$ the solution displays large error.

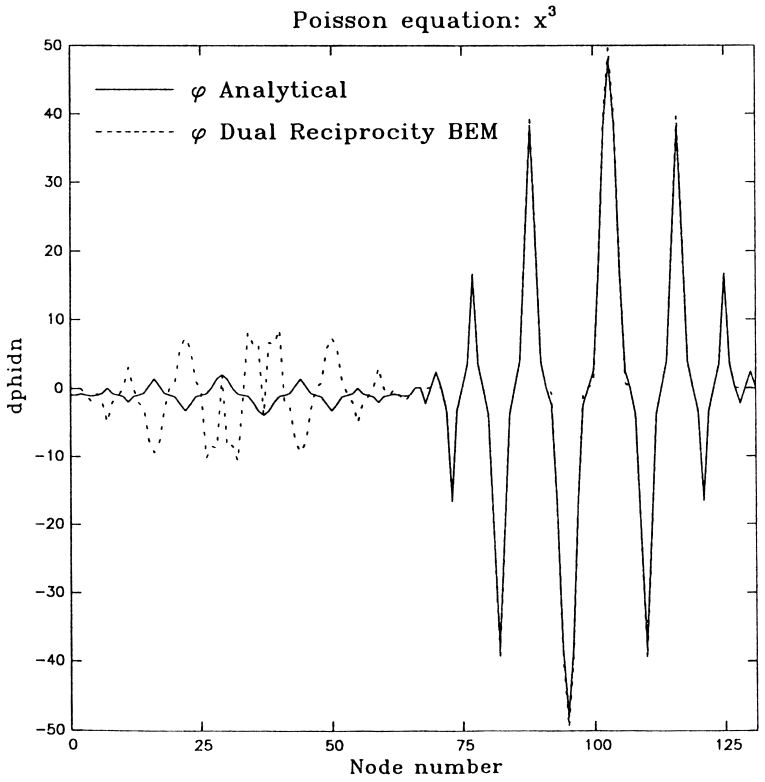

Fig. 10. The solution of the Poisson equation $\nabla^2\phi = x^3$ on the domain of Figure 9. The error in the solution becomes unacceptably large.

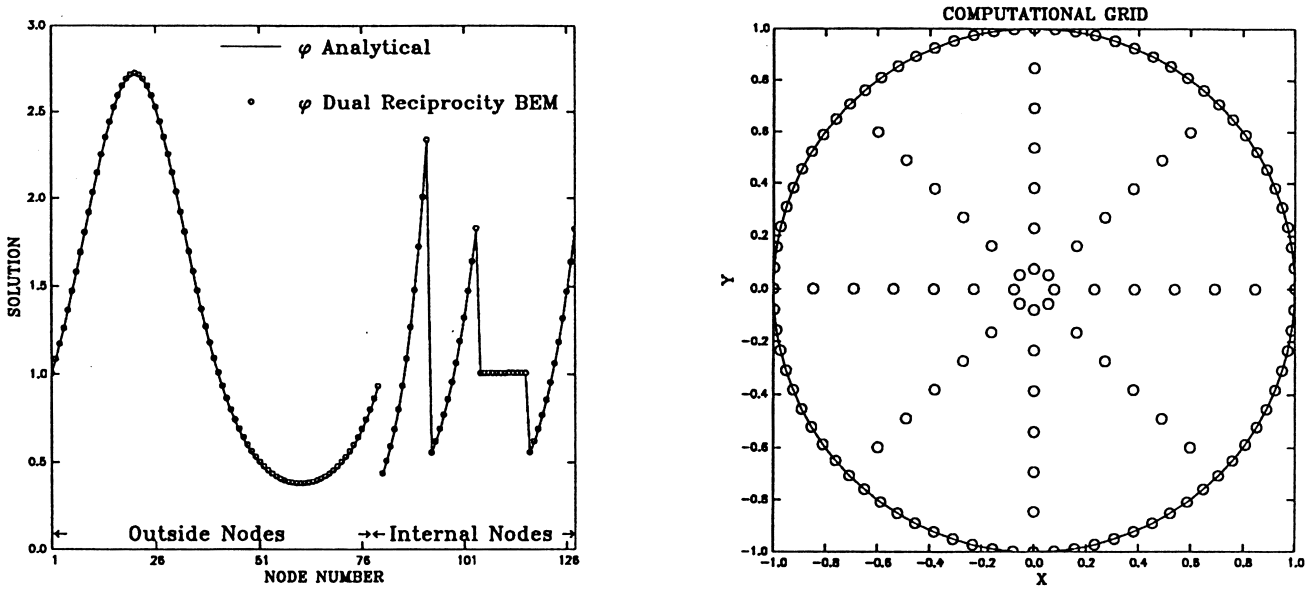

Fig. 11. The solution of the EIT test problem in 2D with $\phi = e^x$. An almost exact match of the solution is obtained using 80 boundary nodes and 48 internal nodes.

panels. In the 2D cases the problem is posed on the unit disk, with 32 external nodes.

5.2.1. EIT test problem for the dual reciprocity code

To test the code on the full problem with a conductivity σ varying in the domain we considered a particular unidimensional exact solution of these equations and tested it in the 2D and fully 3D code. Specializing (1) to 1D, we get

$$\sigma_x \phi_x + \sigma \phi_{xx} = 0. \tag{34}$$

We look for solutions of the form $\phi = \exp(f(x))$, and obtain:

$$\sigma = \exp\big(-\log(f_x) - f\big) = \frac{\exp(-f)}{f_x}. \tag{35}$$

This defines a family of solutions for different choices of f. Substituting for ϕ and its derivatives we select the following test solution for checking our codes

$$f(x) = x,\ \phi = e^x,\ \sigma = e^{-x}. \tag{36}$$

Using the above solution we tested our code **2DynaEIT** for a case with 80 nodes on the boundary and 48 internal nodes. For this discretization the code achieved an almost exact match with the theoretical solution as is illustrated in Fig. 11. The computational grid is also shown in the figure.

The three dimensional code **3DynaEIT** was also tested against this solution, and found to perform satisfactorily. Results for a typical case of a sphere discretized using 146 nodes and 288 panels are shown. The case used 104 extra internal nodes. In this case the average error in the solution is 2%. The analytical and computed solutions along with the computed grid are shown in Fig. 12. A solution with 258 boundary nodes and 240 internal nodes achieved average errors of 0.5%.

6. Inverse problem results

6.1. Identification of constant conductivity regions

Several approaches are available to minimize χ^2. For problems where the error is a smooth function of the parameters, approaches that use derivative information to perform the minimization can reach the solution much faster than those that do not. However, such methods typically require analytical information of the derivatives, to be much faster than techniques that do not require this information. We are currently pursuing work on this problem [18]. In this work we tested three simple methods for minimization, that do not require analytical derivative information [19].

The first was Nelder and Mead's downhill simplex method [19]. In this method an initial 'simplex' is formed by $N + 1$ guesses, where N is the dimension of the minimization problem. Then, using the magnitude of the errors evaluated at the vertices of the simplex, the simplex is subjected to a sequence of stretching, reflection and contraction operations, to reduce the error at these vertices. These operations ensure that as the algorithm converges, the simplex brackets a minimum of the objective function.

The second method was Powell's direction set method [19]. In this method, an initial guess and a set of N independent search directions are provided to the program. In each iteration the method serially performs a sequence of line-minimizations along the directions. At the end of each iteration the method replaces one of the original directions with the line joining two starting and ending points. Care is taken to ensure that the directions remain linearly independent.

The third method tested was the conjugate gradient method. The Jacobian was computed using finite-differences.

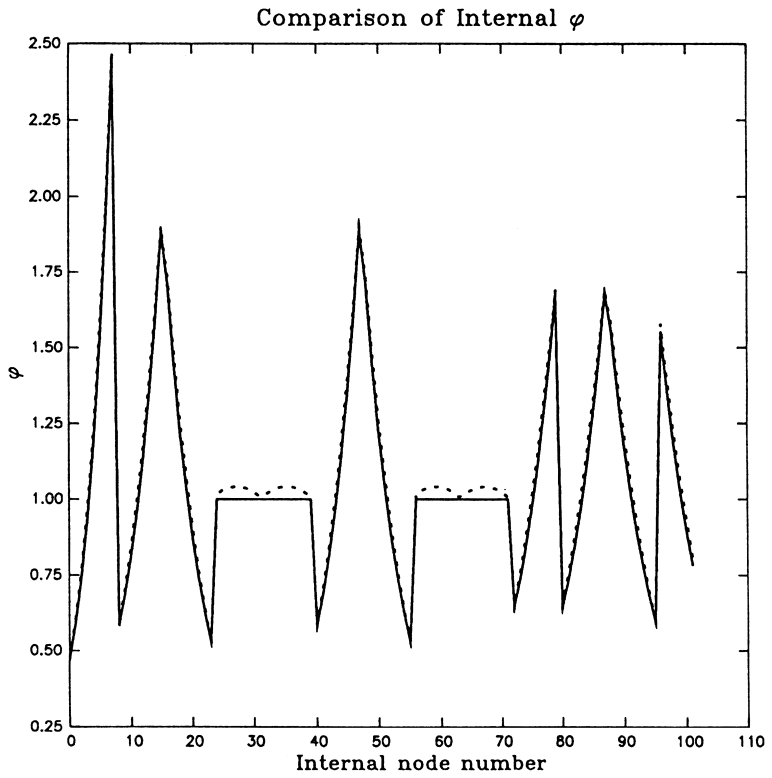

Fig. 12. The solution of the EIT test problem in 3D with $\phi = e^x$. An satisfactory match of the solution is obtained using 146 boundary nodes and 104 internal nodes. The discretization is on the right.

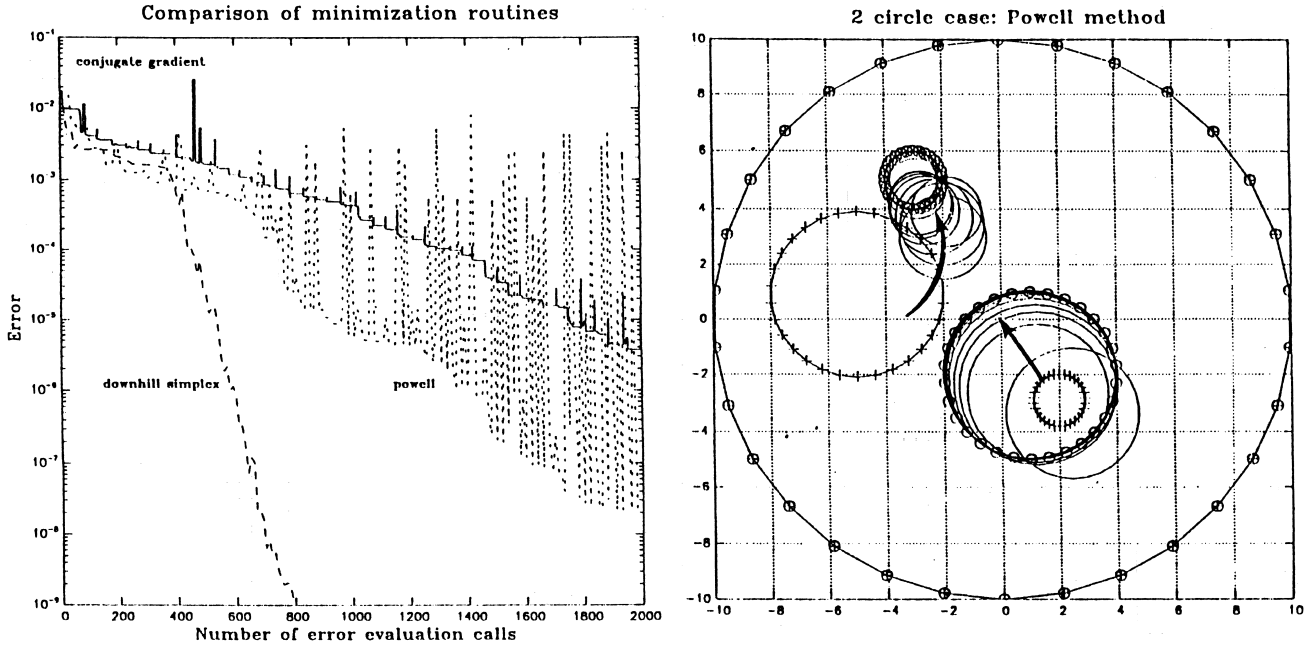

Fig. 13. The figure on the left shows the performance of the downhill simplex, Powell and conjugate gradient methods for a the solution of an EIT inverse problem of the reconstruction of two circular inclusions of zero conductivity. The problem and the sequence of iterates for the Powell method are illustrated in the future on the right. The initial guess is shown using + marks, while the exact solution is shown using open circle.

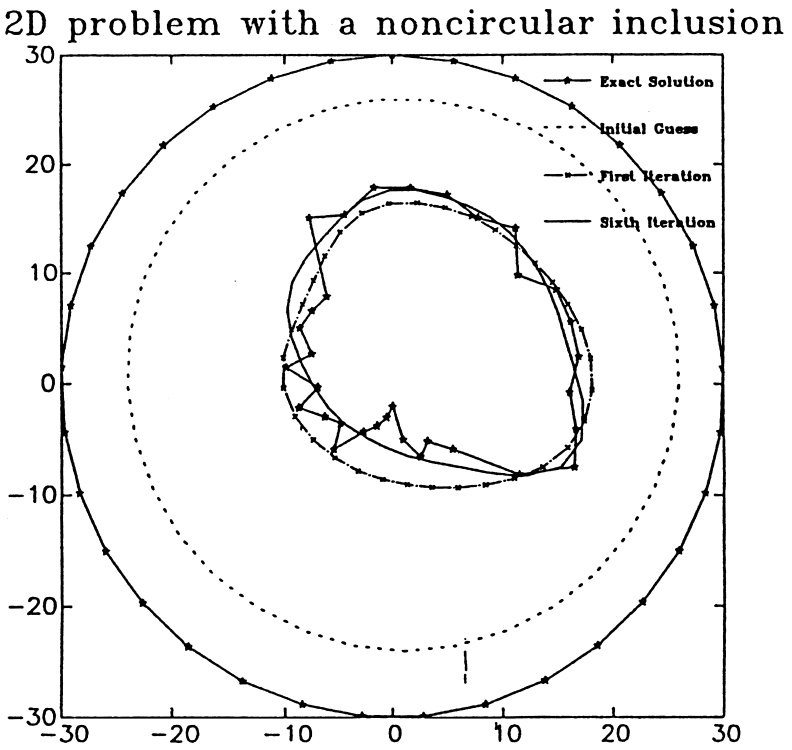

Fig. 14. The reconstruction of an arbitrary shape using a 13 parameter Legendre decomposition. Satisfactory convergence is seen, even after one Powell iteration.

The method was tested to see if its superior convergence rate compensated for the larger number of function evaluations required by the Jacobian evaluation.

6.1.1. Examples

All methods were tested first on the two-dimensional impedance imaging problem of a large cylinder containing one or many smaller inner cylindrical regions of zero conductivity. Since each of the inclusions is modeled as a circle it is parametrized by three parameters — the coordinates of its center and the radius. The methods were observed to converge very well for a variety of inner distributions of circles of varying sizes.

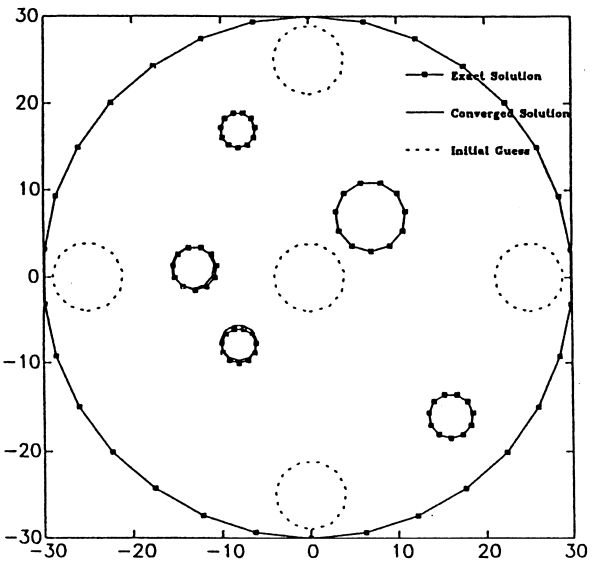

Fig. 15. The reconstruction of five circles of zero conductivity starting from an arbitrary guess. Satisfactory convergence is obtained.

A systematic comparison between the three methods was conducted to choose one for further development. A specific example is shown in Fig. 13. The figure shows the convergence history of the Powell method, and the error convergence history for all methods. Here the nodes on the boundary of the exact solution are marked with open circles, the nodes on the initial guess are marked with + symbols, and the other circles are the converged solutions at the end of every Powell iteration. The other methods have similar convergence histories. The error comparison in Fig. 13 shows that the downhill simplex method requires the least number of evaluations of the error, i.e. the least number of computations of the forward problem to lead to an extremely small r.m.s. error. However, in a practical application where the position and the radius of the sought inclusion are only required within a reasonable amount of precision, the Powell method appears to have the fastest initial convergence rate.

The Powell method was then employed for all subsequent evaluations. The method was tried on a problem in which the inner shape was arbitrary, and characterized by the location of a point, the ‘center’, and a set of Legendre polynomial coefficients given in (32). The shape in Fig. 14 was arbitrarily drawn. As seen in the figure, the Powell

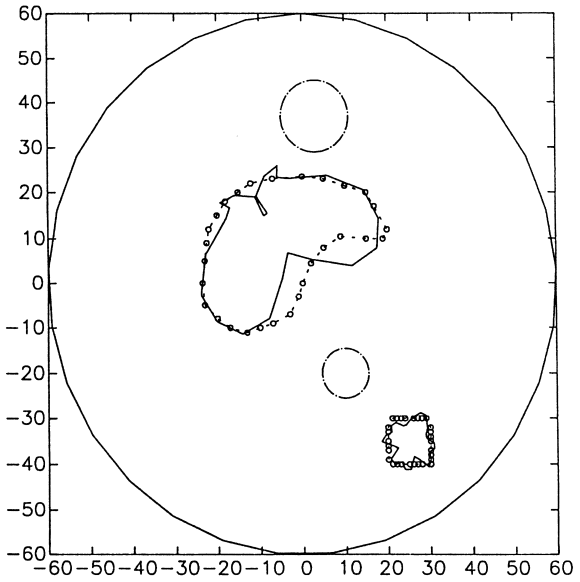

Fig. 16. The reconstruction of two arbitrary shapes (–○–○–) using Legendre polynomial parameterizations. Here the shapes cannot be represented by Legendre polynomials. Despite this a satisfactory convergence is observed. –·– initial guess — converged solution.

method converges satisfactorily within one iteration. This takes less than a minute on our SGI Indigo workstation.

As the number of objects is increased the dimension of the parameter space in which the minimum has to be found increases, and we expect the minimization to be harder. However, we found that our Powell method code is able to achieve the solutions to the problem. In Fig. 15 we present the result of such an inversion for five circles. An excellent convergence can be seen for an initial arbitrary guess (also shown on the figure after about 10 iterations).

In Fig. 16 we show a further attempt at deducing two arbitrary shapes using the Powell method. Again the shapes were entered using arbitrary freehand drawing, and their reconstruction was sought in terms of two sets of 11 Legendre polynomials. Here the Legendre polynomials cannot faithfully represent the drawn shape. However, despite this the method achieved a satisfactory identification.

In the previous examples the number of inclusions was assumed known in the inverse problem solution. In Fig. 17 we show a case where two inclusions are guessed while the domain contains three. The solution identified one inclusion correctly and the other two are approached by an overlapping computed shape. Fig. 18 shows a converse case where the three inclusions are assumed and they approximately identified the regions occupied by the two shapes actually present. These results further emphasize the robustness and flexibility of the method that would allow it to be successful in the real imaging problems. Obviously, more work is required to include the number of inclusions in the parameters to be determined by the inverse problem solution.

In three-dimensions we sought to image regions with zero conductivity inside a larger spherical conducting region. The first example was to correctly find the position and radius of an included sphere of zero conductivity. Excellent convergence is also obtained for this case. Fig. 19 shows a successful solution of a case where the radius of the outer

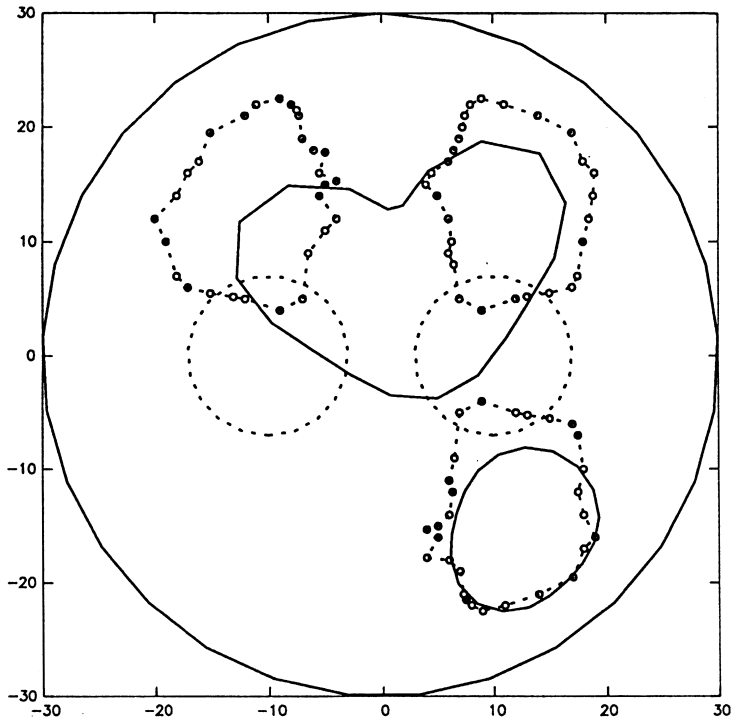

Fig. 17. The identification of three arbitrary shapes (–○–○–) with number of guessed shapes to be two. The second computed shape identifies the region occupied by the two actual shapes. - - - initial guess, —converged solution.

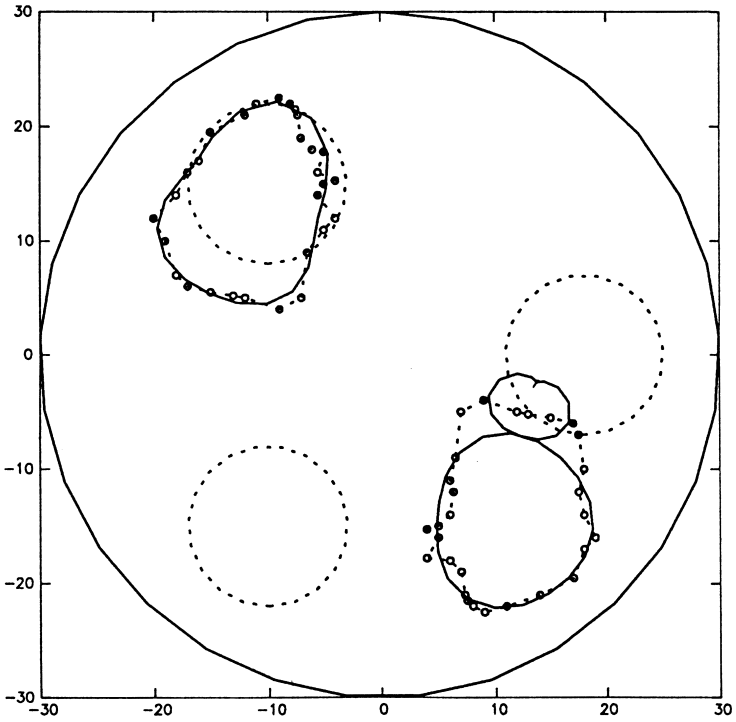

Fig. 18. The identification of two arbitrary shapes with number of guessed shapes to be three. Again the region occupied by the actual shapes is identified by the computed shapes. The line types are the same as in Figure 17.

domain is chosen to be 10, with the inside sphere of radius $R = 2$ at (3,1,−2). The initial guess is $R = 5$ at (2,−3,1). Fig. 20 shows a successful implementation of the code in the case where two spheres were sought. The initial guess of the spheres is shown in a cross section as the starred circles. The final shape is marked with the circle. The figure also shows the cross sections at different iteration numbers.

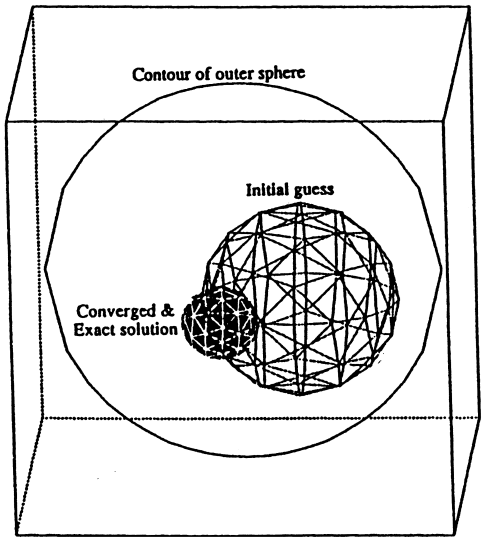

Fig. 19. Reconstruction of a 3D EIT problem. A spherical region of zero conductivity embedded in an outer spherical region is sought to be imaged. The initial guess and the converged solutions are shown.

6.2. Continuous distributions of σ

Concerning the minimization procedure for a continuous σ function we have demonstrated the technique by using Powell's method which was found to converge very quickly in the case of the function distributed were Gaussian bumps on a background of continuous σ. Fig. 21 shows an example. In this case the exact and the initial guessed conductivity distributions were

$$\sigma_{\text{ex}} = 1 + 0.9\exp(-10\left[(x)^2 + (y-0.4)^2\right] \tag{37}$$

$$\sigma_{\text{init}} = 1 + 0.1\exp(-2\left[(x+0.1)^2 + (y+0.2)^2\right]$$

This case converged to within 3 significant figures in 10 Powell iterations (15 minutes CPU time), and to machine precision in 89 Powell iterations (150 minutes CPU time).

Similarly, in three-dimensions, we used Gaussian blobs to model distributions of the conductivity. Fig. 22 shows an example. In this case the conductivity distributions were

$$\sigma_{\text{ex}} = 1 + \exp\left(-25\left[(x-0.3)^2 + (y-0.3)^2 + (z+0.2)^2\right]\right) \tag{38}$$

$$\sigma_{\text{init}} = 1 + 0.5\exp\left(-16\left[x^2 + y^2 + z^2\right]\right)$$

The results are satisfactory.

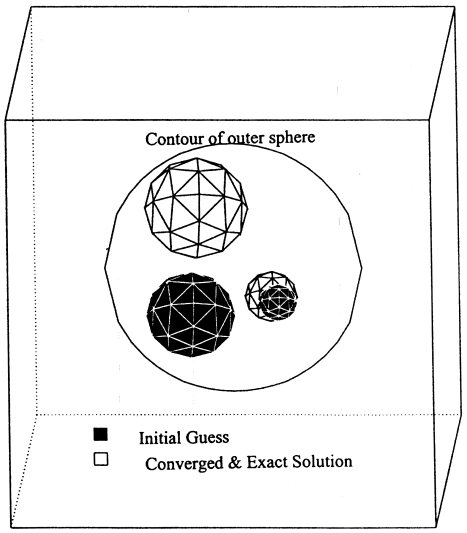

Fig. 20. Reconstruction of a 3D EIT problem. Two spherical regions of zero conductivity embedded in an outer spherical region are sought to be imaged. The left figure shows the successive iterates. Stars are for initial guess, circles for exact and converged solution. Right figure is 3D view of initial guess and converged solution.

7. Summary and conclusions

We have developed several codes based on BEM techniques for studying problems in EIT. These codes can also be applied to the solution of general Poisson and Helmholtz equations. The computational codes for the forward problem were optimized for use in the inverse problem by accounting for the fact that they would be used repeatedly with the same geometrical discretization/electrode set-up but for different distributions of conductivity/inner-surfaces. These optimizations make the codes run much faster.

A new methodology for parametrizing the unknowns of the sought impedance distribution was also developed. This decouples the parametrization from the geometrical discretization of the problem domain, and allows the inclusion of available a priori information. This has the potential of mitigating the ill-posed nature of the inversion considerably. Different alternative decoupled parametrizations for the problems were developed. Further, for problems where sharp interfaces are sought this approach includes the information in the formulation, and eliminates the need for a posteriori image enhancement.

The forward problem codes were embedded in simple standard minimization schemes (downhill simplex, Powell and Conjugate Gradient) and found to converge to the exact

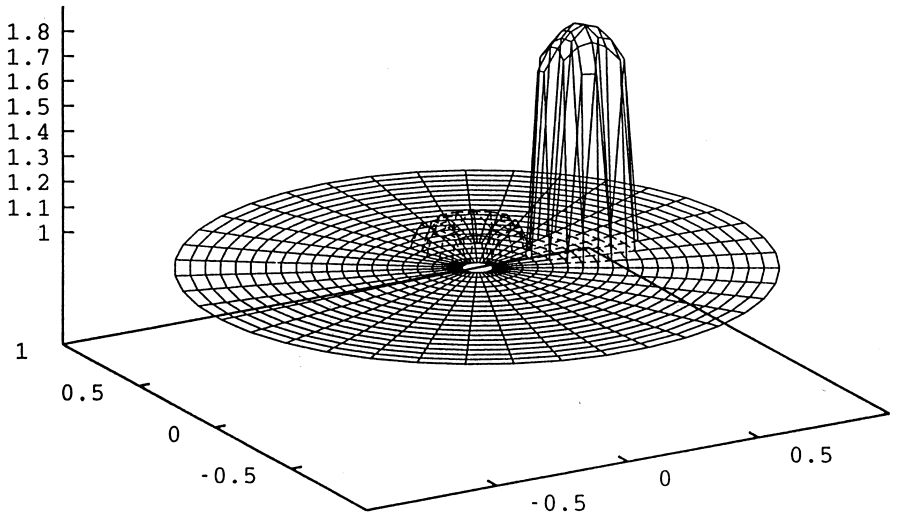

Fig. 21. Reconstruction of σ in 2D given by a Gaussian bump on a constant background.

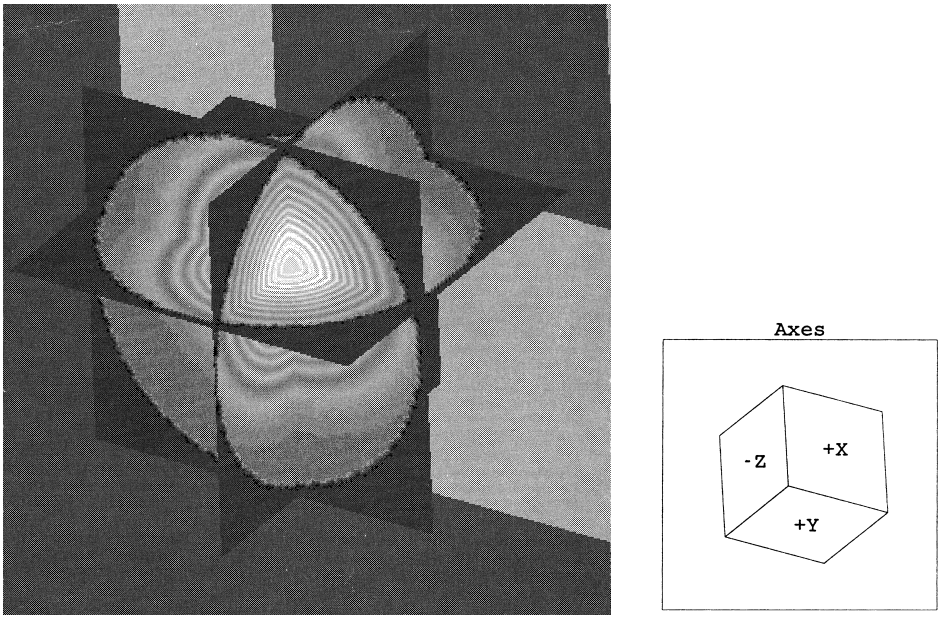

Fig. 22. Reconstruction of σ in 3D given by a Gaussian blob on a constant background. Contours of constant σ on the planes $x = 0.3$, $y = 0.3$, and $z = -0.2$ are shown. The exact and converged solutions are indisintugishable.

distribution, for imaging multiple circles and spheres respectively in 2D and 3D, for the identification of multiple arbitrary shapes in 2D, and for imaging continuous conductivity distributions in 2D and 3D.

The presented results are the first application of DRBEM techniques to Electrical Impedance Tomography. Further, the 3D EIT reconstructions are, to our knowledge, the first fully three-dimensional direct reconstructions. Earlier researchers had attempted to obtain slice wise reconstructions, which would then be patched together, or obtain heuristic 3D reconstructions. We have successfully demonstrated that BEM techniques can lead to very efficient algorithms for EIT. In ongoing work we are aiming at more efficient solution of the inverse problem of EIT. [18] Future work will aim at an experimental implementation of the algorithms.

References

[1] Holder D, editor. Clinical and physiological applications of electrical impedance tomography. London: UCL Press, 1993.
[2] Quinto ET, Cheney M, Kuchment P, editors. Tomography, impedance imaging, and integral geometry. Providence, RI: American Mathematical Society, 1994.
[3] Barber B, Brown BH. Applied potential tomography. J Phys E Sci Instrum 1984;17.
[4] Santosa F, Vogelius M. A backprojection algorithm for electrical impedance imaging. SIAM J Appl Math 1990;50:216–243.
[5] Yorkey TJ, Webster JG, Tompkins WJ. Comparing reconstruction algorithms for electrical impedance tomography. IEEE Transactions on Biomedical Engineering 1987;BME34(II).
[6] Hua P, Woo EJ, Webster JG, Tompkins WJ. Iterative reconstruction methods using regularization and optimal current patterns in electrical impedance tomography. IEEE Trans on Medical Imaging 1991;10:621–628.
[7] Somersalo E, Cheney M, Isaacson D. Existence and uniqueness for electrode models for electric current computed tomography. SIAM J Appl Math 1992;52:1023–1040.
[8] Jones OC, Lin J-T, Shu H, Ovacik L, He Y. Impedance imaging relative to binary mixtures. In: Roco MC, Crowe CT, Joseph DD, Michaelides EE, editors. Proceedings, liquid solid flows, ASME FED-Vol. 189. New York: ASME, 1994.
[9] O'Hern TJ, Torczynski JR, Ceccio SL, Tassin AL, Chahine GL, Duraiswami R, Sarkar K. Development of an electrical impedance tomography system for an air–water vertical bubble column. In: Forum on measurement techniques in multiphase flows, FED-Vol. 233. New York: ASME, 1995:531–537.
[10] Chahine GL, Duraiswami R. Dynamical interactions in a multi-bubble cloud. ASME J Fluids Engg 1992;114:680–686.
[11] Chahine GL, Duraiswami R. Boundary element method for calculating 2D and 3D underwater explosion bubble behavior in free water and near structures. Naval Surface Warfare Center, White Oak Detachment Technical Report NSWCDD/TR-93/44, 1994.
[12] Chahine GL, Perdue TO. A 3D boundary element method for explosion bubble dynamics. In: Wang TG, editor. Drops and bubbles, AIP Conference Proceedings, 197, 1989:169–187.
[13] Partridge PW, Brebbia CA, Wrobel LC. The dual reciprocity boundary element method. London: Elsevier, 1992.
[14] Powell MJD. The theory of radial basis function approximation in 1990. In: Light W, editor. Advances in numerical analysis, vol. II. Oxford: Clarendon Press, 1992:105–210.
[15] Buhmann MD, Ron A. Radial basis functions: L^p approximation orders with scattered centers. In: Laurent P-J, Le Mehaute A, Schumaker LL, editors. Wavelets, images and surface fitting. Wellesley, MA: A.K. Peters Ltd., 1994:93–112.
[16] Dobson DC, Santosa F. An image-enhancement technique for electrical impedance tomography. Inverse Problems 1994;10:317–334.
[17] Rudin L, Osher S. Feature-oriented image enhancement using shock filters. SIAM J Numer Anal 1990;27:919–940.
[18] Duraiswami R, Sarkar K, Prabhukumar S, Chahine GL. BEM methods for efficient 2D and 3D electrical impedance tomography. NSF Phase I SBIR Final Report, Grant DMI-9461681. Also, Dynaflow, Inc. Technical Report 95006-1, August 1995.
[19] Press WH, Teukolsky SA, Vetterling WT, Flannery BP. Numerical recipes, 2nd edn. Cambridge: Cambridge University Press, 1992.

[20] Webster JG. Electrical impedance imaging. In: Webster JG, editor. Electrical impedance tomography. New York: Adam Hilger, 1990.
[21] Jones OC, Lin J-T, Shu H, Ovacik L, He Y. Impedance imaging relative to binary mixtures. In: Roco MC, Crowe CT, Joseph DD, Michaelides EE, editors. Proceedings, Liquid Solid Flows, ASME FED-Vol. 189. New York: ASME, 1994.
[22] Duraiswami R. Bubble nuclei measurement using an inverse acoustic scattering technique. In: Cavitation and multiphase flow forum. Washington, DC: ASME, FED, 1993.
[23] Cheng AH-D, Grilli S, Lafe O. Dual reciprocity boundary element based on complete set global shape functions. In: Brebbia CA, Rencis JJ, editors. Boundary elements XV. 1993:343–357.